Breakdown of Spin-to-Helicity Locking at the Nanoscale in Topological Photonic Crystal Edge States

S. Arora[1], T. Bauer[1], N. Parappurath[2], R. Barczyk[2], E. Verhagen[2], and L. Kuipers[1,*]

[1]*Kavli Institute of Nanoscience, Delft University of Technology, 2600 GA Delft, Netherlands*
[2]*Center for Nanophotonics, AMOLF, Science Park 104, 1098 XG Amsterdam, Netherlands*

We measure the local near-field spin in topological edge state waveguides that emulate the quantum spin Hall effect. We reveal a highly structured spin density distribution that is not linked to a unique pseudospin value. From experimental near-field real-space maps and numerical calculations, we confirm that this local structure is essential in understanding the properties of optical edge states and light-matter interactions. The global spin is reduced by a factor of 30 in the near field and, for certain frequencies, flipped compared to the pseudospin measured in the far field. We experimentally reveal the influence of higher-order Bloch harmonics in spin inhomogeneity, leading to a breakdown in the coupling between local helicity and global spin.

Robust unidirectional transport of photonic states with coherent and highly efficient light-matter coupling is a luring proposition for large-scale on-chip quantum networks [1,2]. Unidirectional photon emission is achieved, in general, by strong coupling of a quantum emitter supporting a circularly polarized dipole moment to photonic states with a corresponding local polarization orientation (helicity) [3–6]. This results in a chiral quantum optical interface owing to spin-momentum locking [7]. However, many practical realizations of such chiral interfaces exhibit only a finite spin-to-direction coupling. These realizations are susceptible to disorder and defects [8]. More so, unambiguous spin-dependent transport of quantum information from chiral emitters requires an explicit account of the local structure of the edge state's optical spin density profile to achieve high directional coupling [5,9–18].

One class of systems that has been proposed in the context of robust spin-dependent transport, is the photonic crystal-based analog of topological insulators which emulate the quantum spin Hall effect (QSHE) [19]. They feature two symmetry-protected edge states at the interface between a topologically trivial and nontrivial lattice [20,21]. Experimental as well as numerical realizations have shown that the two edge states each exhibit a unique pseudospin due to the different topological invariants of the supporting bulk bands, that makes photonic transport robust to defects and sharp corners [17,22,23]. This transport relies on pseudospin coupling to the far-field (FF) helicity to ensure and maximize photon unidirectionality [24]. Leveraging the helicity supported by these systems has enriched applications for quantum entanglement [10] and quantum spin circuits [25–29]. However, it is essential to determine the exact relation between field helicity and edge state pseudospin.

In this Letter, we examine the near field of edge states in topological photonic crystals (TPCs) to comprehensively study the (local) chiral information. With aperture-based phase- and polarization-resolved near-field optical microscopy (NSOM) [30], we collect the orthogonal in-plane polarization components of the electric field using a heterodyne detection scheme and determine the underlying spatially varying spin density. We experimentally verify that the inhomogeneity in optical spin density follows the Bloch periodicity of the lattice. By experimentally accessing the different Bloch harmonics (BHs) that together form the symmetry-protected edge state, we show that accounting for the individual contribution of each higher-order BH breaks the coupling between pseudospin and helicity of the edge state.

Following the shrink-and-grow design [20,21,31], we realize a TPC interface on a silicon-on-insulator platform by deforming a graphenelike hexagonal lattice with six equilateral triangular holes. While the unperturbed lattice features a doubly degenerate Dirac cone at the Γ point in the dispersion diagram, this degeneracy is lifted in two ways [see Fig. 1(a)]: on one side of the interface, the holes are concentrically shifted inwards, called the shrunken lattice (L_S), while on the other side, the holes are shifted concentrically outwards, labelled as expanded lattice (L_E). The geometrical transformations keep the global C_6 symmetry of each lattice unaltered. The band structure of L_S and L_E both reveal a direct bandgap at the Γ point. For L_S, the shape of the electric field in the lower band resembles "p"-like orbitals and the upper band resembles "d"-like orbitals, whereas for L_E, the mode symmetries of the upper and lower band is inverted [20]. The different intracell and intercell coupling strengths between neighboring sites in the two lattices imparts a nontrivial nature to the expanded

lattice [32]. The interface of L_S and L_E supports two counterpropagating edge states that traverse the band gap around the Γ point [20,21]. These edge states are robust against backscattering and offer unidirectional transport, provided no scattering between pseudospins occurs. The TPC reported in this Letter is different from a photonic crystal emulating the quantum valley Hall effect [33–37], as the latter supports edge states that lie around the high-symmetry points K and K' of the Brillouin zone. Since the QSHE TPC edge states traverse the Γ point, the counter-propagating modes lie above the light cone and therefore couple to FF radiation. This makes them accessible to far-field spectroscopic investigations [22,31,38]. Here, the polarization of the light scattered to the FF shows a near-unity optical spin and can be directly linked to the state's pseudospin [31,39,40]. However, the radiative FF does not contain the full complex information of the evanescent electromagnetic field since it only takes into account the plane waves within the light cone [41,42] and a detailed account of the full local field is imperative for ensuring chiral light-matter interactions on the nanoscale.

To experimentally investigate the spin character of the TPC interface rigorously, we fabricate a lattice featuring an armchair (AC) interface. Figure 1(a) shows the unit cell structure on both sides of the interface. We measure the complex in-plane electric field distribution $\mathbf{E}$ using a phase- and polarization-resolving near-field scanning optical microscope. The light propagation along the interface is schematically visualized in Fig. 1(b). Here, we distinguish the two typical evaluation regimes of the electromagnetic (EM) field: near (NF) and radiative far (FF). The former defines the component of the EM field directly above the crystal surface, constituting the decaying evanescent field as well as the radiative field ($\mathbf{E_{rad}}$) of the propagating edge state. The latter typically forms at distances of multiple wavelengths away from the interface and is associated with only $\mathbf{E_{rad}}$. In Fig. 1(c), we depict the measured electric field amplitude at an excitation wavelength of $\lambda = 1520$ nm. A highly structured field is visible. The mode amplitude dimi-nishes while propagating from left to right as shown in the full electromagnetic field distribution in the Supplemental Material, Fig. S1 [43] and is associated with radiative coupling to the FF [31,39,40]. A zoom-in of the full near and radiative field is shown in Figs. 1(c) and 1(d). The field profile around the AC interface [indicated by the solid gray line in Fig. 1(c)] resembles a Bloch wave [44] with pockets of high and low field amplitude forming a hexagonal pattern that repeats with lattice periodicity a along the propagation direction $+x$. The dominant part of the field is confined to the interface. The transverse extent of the edge state shows that the field extends further into the L_S bulk than in L_E (see Supplemental Material Fig. S1 [43] for more information on longitudinal and transverse extent). This asymmetry in evanescent tails is consistent with the relative width of the photonic band gap of the lattices,
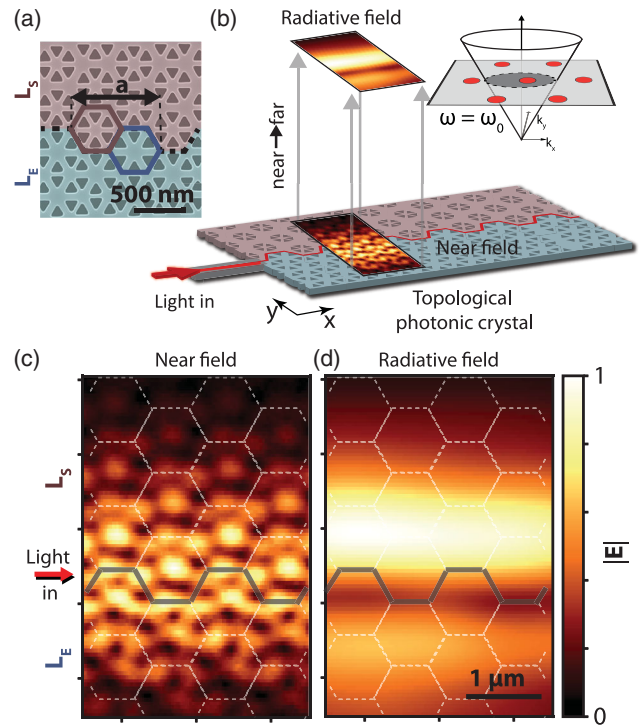

FIG. 1. (a) Scanning electron micrograph (SEM) of the topo-logical interface in the fabricated sample with the color-coded regions depicting the shrunken L_S (red) and expanded L_E (blue) lattices. The lattice periodicity is $a = 880$ nm. (b) Schematic representation of the TPC lattice with overlaid near- and far-field amplitudes of the electromagnetic field. Inset: Schematic repre-sentation of the reciprocal space of an edge state (frequency $\omega = \omega_0$) with its typical hexagonal pattern of intensity peaks together with the 3D light cone of air ($\omega = ck$). The dashed circle at the intersection of the light cone and the reciprocal space of the edge states represents the largest spatial frequencies of the edge state that can couple to the far field. Close-up of the normalized in-plane electric (c) near-field and (d) radiative field amplitude in the TPC featuring an armchair interface at $\lambda = 1520$ nm with the light launched into the structure from the left (indicated by the red arrow). The dashed hexagonal pattern outlines the underlying crystal lattice.

which is larger for L_E. The structured NF information is transformed to the radiative FF of the edge state by limiting the collected wave vector range to lie within the light cone using Fourier filtering. This is depicted in the inset of Fig. 1(b), which shows a schematic of the reciprocal space of the edge state with intensity peaks in a hexagonal pattern for an exemplary excitation frequency ω_0. The single peak inside the dashed circle on the 2D projection of the light cone for ω_0 constitutes the radiative FF. In contrast to Fig. 1(c), where the amplitude antinodes follow the under-lying crystal structure, the FF amplitude is homogeneous along the TPC interface [see Fig. 1(d)]. For a Bloch mode propagating in the x direction, an infinite set of BHs in reciprocal space (with spatial frequencies separated by multiples of $2\pi/a$, where a is the lattice periodicity)

together form the detailed near-field structure of an edge state in real space. Each BH contributes to the mode amplitude with a certain weight that leads to the field variations in each unit cell. In the y direction the periodicity of the lattice causes peaks in reciprocal space with the same spacing, corresponding to the lateral mode profile of the edge state [45]. Only spatial frequencies within the so-called light cone [dashed circle in inset Fig. 1(b)] can couple to the FF. Here, this fundamental BH radiates to the FF as it couples with the continuum of free-space air modes. We obtain it by filtering to the single in-plane k vector inside the light cone. A Fourier transform of these spatial frequencies yields the radiative field [Fig. 1(d)]. Predictably, the dominant field energy in the FF lies more on the shrunken side of the interface, consistent with NF observations and the corresponding size of the bulk band gaps. An evanescent field strongly confined to the interface, propagating in the $+x$ direction and decaying in the y direction, implies the existence of transverse spin [46–49] with positive and negative helicity mirrored at the interface. For our C_6 symmetric lattice, this results in the dominance of one designated helicity that is locked to the direction of mode propagation. The calculated transverse optical spin of the evanescent field is therefore a nonzero value. However, the spin distribution of the mode in the NF and FF differs.

From the experimentally measured in-plane complex electric field, we reconstruct the spin density distribution $\sigma_z(x, y) = \text{Im}[\mathbf{E}^*(x, y) \times \mathbf{E}(x, y)]_z$ [47], where $\mathbf{E}^*(x, y)$ is the complex conjugate of the electric NF and Im indicates that only the imaginary part of the resultant complex vector field is extracted. The derived quantity is visualized in Fig. 2 which depicts the experimentally measured [(a),(b)] and numerically calculated [(c),(d)] $\sigma_z(x, y)$. For the evanescent field, σ_z is the expectation value of the helicity of light and it directly translates to the *local* field polarization state of the photonic TE-like mode as a result of spin-orbit interactions. The NF σ_z depicted in Fig. 2(a) reveals a highly structured σ_z distribution. A periodic

pattern of $+\sigma_z$ and $-\sigma_z$ is observed, that repeats with a periodicity of a in the propagation direction and $a/\sqrt{3}$ in the transverse direction. Close to the center of any given unit cell indicated by dashed lines in Fig. 2(a), antinodes of $+\sigma_z$ are prominent, whereas around the outlines of the unit cell, the sign of σ_z flips. This spin flip within a unit cell confirms that the local handedness of a topological edge mode's polarization state is non-uniform. The local inhomogeneity of the spin density $\sigma_z(x, y)$ in the NF

$$\mathbf{E}_{\mathbf{NF}}(x, y) = \iint_{-\infty}^{\infty} \tilde{\mathbf{E}}(k_x, k_y) e^{i[k_x x + k_y y]} dk_x dk_y, \quad (1)$$

which takes into account all spatial frequencies, completely vanishes in the FF

$$\mathbf{E}_{\mathbf{rad}}(x, y) = \iint_{k_x^2 + k_y^2 < k_0} \tilde{\mathbf{E}}(k_x, k_y) e^{i[k_x x + k_y y]} dk_x dk_y \quad (2)$$

[shown in Fig. 2(b)], where $k_0 = \omega/c$. For an excitation wavelength of $\lambda = 1520$ nm, only $+\sigma_z$ is visible close to the interface. This is in perfect agreement with reports of near-unity spin density in FF measurements [31]. Comparing both regimes to numerical simulations in Figs. 2(c) and 2(d) reveals an excellent agreement of the σ_z distribution for the NF as well as the FF case, respectively. To understand the origin of the observed spatial variations and difference in NF and FF, we undertake a detailed analysis of the edge states in momentum space.

We investigate the dissimilarity in the NF and FF optical spin density distribution by analysing the *global* optical spin $S = \iint \sigma_z(x, y) dx dy$ of the edge state over its full band dispersion, representing the integrated helicity of the interface mode. Figure 3 shows the calculated eigenmodes of the AC interface for both regimes. Figures 3(a) and 3(b) both show a linear dispersion for the edge states that lie within the band gap and cross at the Γ point. The edge states are disconnected from the top and bottom bulk bands and recombine at the Brillouin zone edge. We notice an anticrossing of 0.1 THz, predicted by the extended tight-binding model [50]. This is a result of spin-spin scattering due to coupling of the counterpropagating edge states governed by the local C_6 symmetry breaking at the interface of the TPC. For Figs. 3(a) and 3(b) the color scale represents the sign of the optical spin S. The minimum and maximum extent of the scale for the two subplots are distinctly different. Figure 3(a) shows the dispersion obtained by calculating S from the in-plane field distributions and is referred to as the NF optical spin (S_{NF}). As expected, the degenerate counterpropagating edge states exhibit opposing helicity. However, we observe that this helicity is flipped in Fig. 3(b), where we plot the FF spin (S_{FF}) of the edge states. The linear state with negative S_{NF} possesses positive S_{FF} and vice versa. Moreover, the S_{FF} exhibits a near-unity value, more than an order of
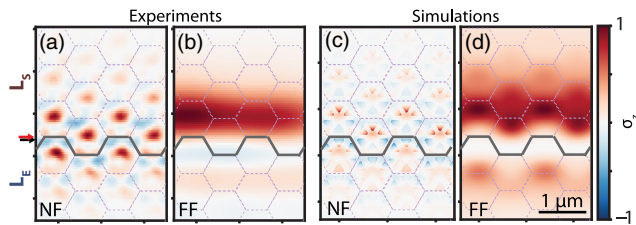

FIG. 2.   (a) Experimentally measured NF spin density σ_z of the AC-edge mode over two unit cells for an excitation wavelength of $\lambda = 1520$ nm. (b) Experimentally measured FF spin density over the same extent as in (a), realized by filtering out the nonradiative wave vectors of the field shown in (a). (c) Numerically calculated spin density for $k_x = 0.16$ $(2\pi/a)$ with (d) displaying the spin density for numerical simulations in the FF. The solid gray line indicates the armchair interface while the dashed hexagonal pattern outlines the underlying crystal lattice.
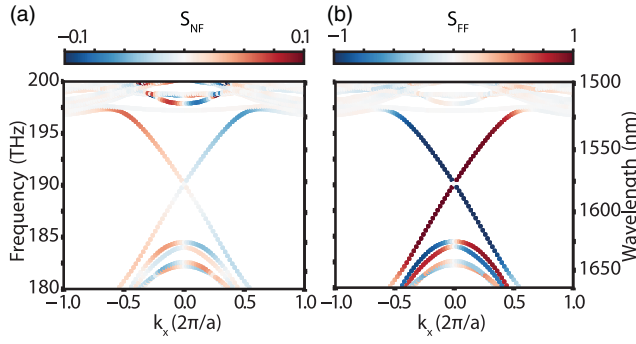
FIG. 3. Numerically simulated dispersion relation where the edge state eigenfrequencies are color coded with the estimated (a) near-field and (b) far-field optical spin S.

magnitude larger than the maximum $S_{\mathrm{NF}} = \pm 0.056$. The tight-binding approach dictates that the pseudospin for each edge state is uniquely linked to its FF helicity. On the other hand, the much lower S_{NF} and the spin flip suggest that the pseudospin of the full electromagnetic mode of the edge state is in fact not uniquely linked to a designated S_{NF}. The principal difference between NF and FF observations stems from the fact that the evanescent NF contains information from all higher-order BHs, which are unaccounted for in the FF. To better understand this intriguing spin-flip transition, we investigate the spin of the individual BHs.

The origin of the spatially varying spin distribution of the Bloch periodic structure is confirmed by performing a two-dimensional Fourier transform $\mathcal{F}(k_x, k_y)$ (shown in Fig. 4) of the measured complex field amplitude as visualised in Supplemental Material Fig. S1 [43], for an excitation wavelength $\lambda = 1560$ nm. The high-intensity peaks arranged in a hexagonal pattern in reciprocal space are the result of the underlying C_6 symmetry. A small amount

of air-guided, unwanted stray light that is not part of the edge state mode, skims along the surface of the photonic crystal. Because it propagates in air parallel to the surface, its spatial frequency lies exactly on the circular ring originating from the light cone (indicated as white dashed circle in Fig. 4) and can therefore easily be removed by Fourier filtering. For the chosen wavelength, within this light cone lies a central peak at $k_y = 0$ that corresponds to the part of the Bloch mode radiating to the FF. Along k_x at multiples of $2\pi/a$, clusters of peaks are seen that correspond to the different BHs building up the intricate NF subwavelength structure of the edge state. An excellent signal-to-background ratio (S/B) of 40 dB is obtained in our experiment that allows us to resolve seven different BHs. These BHs, each contributing with different weights, together form the edge state mode which obeys Bloch's theorem [45]. Individual contributions of individual BH to S hold utmost significance in understanding the inhomogeneity in the underlying spin structure.

We restrict our analysis in building up BH contributions by increasing the Fourier filter width in momentum space along k_x. In Figures 5(a) and 5(b), the first column represents the S originating from the fundamental BH ($k_{\bar{0}}$) which extends from $k_x = [-0.5, 0.5]$ in units of $(2\pi/a)$, while the consecutive columns represent to S corresponding to all higher-order BHs up and including the BH indicated in the horizontal axis label, i.e., the wave vector range $k_{\bar{n}} \triangleq [-1, 1] * (n + 0.5)$ in units of $(2\pi/a)$ (see right inset of Fig. 4). The position of the Γ-point crossing differs in Figs. 5(a) and 5(b) due to slight variations in geometric parameters of the fabricated photonic crystal device. The quantitative analysis of the BH contribution to the optical spin is performed by first isolating BHs of certain width along k_x, applying an inverse Fourier transform to obtain the real-space field amplitude and
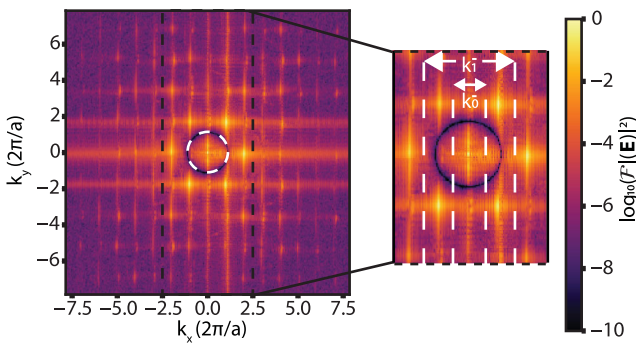

FIG. 4. Two-dimensional Fourier representation of the experimentally measured electric field amplitude of the TPC edge mode at a wavelength of $\lambda = 1560$ nm, with the amplitude shown in logarithmic scale. The reciprocal lattice vectors are periodically separated in the propagation direction (k_x) in units of $2\pi/a$, where a is the lattice constant of the armchair edge. The white dashed circle represents the light cone in air. Right inset: Zoom-in of momentum space restricted to show the fundamental ($k_{\bar{0}}$) and first higher-order BH ($k_{\bar{1}}$).
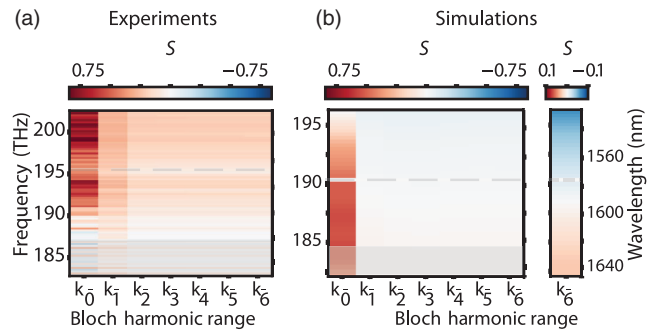

FIG. 5. Buildup of spin-dependent contributions of the BHs from (a) experiment and (b) numerical simulations, evaluated over several higher-order BH ranges. Right inset: Spin-dependent contribution for the largest evaluated BH range which extends from $k_x = [-6.5, 6.5]$ with a saturated color scale. The gray dashed line indicates the frequency of the Γ-point crossing. The grayed out region extending below 184.4 THz depicts the lower band edge.

subsequently calculating S. For $k_{\bar{0}}$, S reflects the near-unity value that has been previously reported in FF measurements [31]. Taking an exemplary frequency of 188.92 THz in simulations, the radiative FF helicity $S_{k_{\bar{0}}} = 0.53$. As the filter width in k_x increases along the x axis in Fig. 5, the optical spin S of the edge state reduces drastically (at exemplary frequency the integrated NF spin $S_{k_{\bar{5}}} = -3.931 \times 10^{-4}$). We acknowledge that the distinct difference between exact values of S for experiment and numerical calculation arise partly by the polarization sensitivity of the NF probe [51]. Nevertheless, $S_{k_{\bar{x}}}$ undergoes a clear reduction from the fundamental BH column represented as $k_{\bar{0}}$ to the first higher-order BH represented as $k_{\bar{1}}$, as shown in Fig. 5. For simulations, the calculated average reduction factor of S in the near field is 30. This means that S cannot be a deterministic helicity parameter of the edge interface when including more than the fundamental BH since a one-on-one relation between local spin and helicity is no longer valid. For every additional higher BH contribution starting at $k_{\bar{1}}$ and above along the x direction, the spin-momentum coupling breaks down to such an extent that it results in a sign flip as is evident from the sign switch (positive to negative value) with increasing frequency in the right inset of Fig. 5(b). It is important to note that the color bar for the inset was saturated to ± 0.1 to make the sign flip for $k_{\bar{1}}$ and above visible. The extrema of the numerically simulated S is ± 0.57. Therefore, we observe that already the first higher-order BH contribution to the *global* optical spin completely breaks down pseudospin-momentum coupling.

In summary, we experimentally visualize the intricate spin density distribution of symmetry-protected edge states in topologically nontrivial photonic crystals that lie above the light line, using a NF microscope. We demonstrate that spin in such photonic systems no longer retains its unique handedness in comparison to electronic systems, where *s* must always be a good quantum number. We report that even the contribution of the first-order BH unambiguously flips the sign for certain excitation frequencies. Consequently, a *priori* knowledge of detailed high spin density locations obtained from NF information will improve chances of precise positioning of quantum emitters along chiral interfaces. Without this knowledge, spin-polarized emission will result in mixing of pseudospin edge states, and therefore reduce the desired network efficiency. Thus, this finding needs to be accounted for in the architectures of future topological photonic quantum networks and it provides a pathway towards engineering truly robust topologically protected chiral interfaces.

* l.kuipers@tudelft.nl
[1] J. Borregaard, A. S. Sørensen, and P. Lodahl, Adv. Quantum Technol. **2**, 1800091 (2019).
[2] H. Pichler and P. Zoller, Phys. Rev. Lett. **116**, 093601 (2016).
[3] R. J. Coles, D. M. Price, J. E. Dixon, B. Royall, E. Clarke, P. Kok, M. S. Skolnick, A. M. Fox, and M. N. Makhonin, Nat. Commun. **7**, 11183 (2016).
[4] I. Söllner, S. Mahmoodian, S. L. Hansen, L. Midolo, A. Javadi, G. Kiršanske, T. Pregnolato, H. El-Ella, E. H. Lee, J. D. Song, S. Stobbe, and P. Lodahl, Nat. Nanotech. **10**, 775 (2015).
[5] A. B. Young, A. C. T. Thijssen, D. M. Beggs, P. Androvitsaneas, L. Kuipers, J. G. Rarity, S. Hughes, and R. Oulton, Phys. Rev. Lett. **115**, 153901 (2015).
[6] K. Y. Bliokh, F. J. Rodríguez-Fortuño, F. Nori, and A. V. Zayats, Nat. Photonics **9**, 796 (2015).
[7] T. Van Mechelen and Z. Jacob, Optica **3**, 118 (2016).
[8] B. Orazbayev and R. Fleury, Nanophotonics **8**, 1433 (2019).
[9] M. Proctor, R. V. Craster, S. A. Maier, V. Giannini, and P. A. Huidobro, ACS Photonics **6**, 2985 (2019).
[10] W. M. Deng, X. D. Chen, F. L. Zhao, and J. W. Dong, J. Opt. **20**, 014006 (2018).
[11] H. Wang, S. K. Gupta, B. Xie, and M. Lu, Front. Optoelectron. **13**, 50 (2020).
[12] Y. Mazor and A. Alù, Phys. Rev. Applied **14**, 014029 (2020).
[13] J. Petersen, J. Volz, and A. Rauschenbeutel, Science **346**, 67 (2014).
[14] M. Proctor, X. Xiao, R. Craster, S. Maier, V. Giannini, and P. Arroyo Huidobro, Photonics **7**, 81 (2020).
[15] S. S. Oh, B. Lang, D. M. Beggs, D. L. Huffaker, M. Saba, and O. Hess, in *CLEO Pacific Rim Conference 2018, Hong Kong, China* (Optical Society of America, 2018), p. Th4H.5.
[16] D. G. Baranov, R. S. Savelev, S. V. Li, A. E. Krasnok, and A. Alù, Laser Photonics Rev. **11**, 1600268 (2017).
[17] M. Jalali Mehrabad, A. P. Foster, R. Dost, E. Clarke, P. K. Patil, A. M. Fox, M. S. Skolnick, and L. R. Wilson, Optica **7**, 1690 (2020).
[18] L. Sapienza, M. Davanço, A. Badolato, and K. Srinivasan, Nat. Commun. **6**, 7833 (2015).
[19] M. Z. Hasan and C. L. Kane, Rev. Mod. Phys. **82**, 3045 (2010).
[20] L. H. Wu and X. Hu, Phys. Rev. Lett. **114**, 223901 (2015).
[21] S. Barik, H. Miyake, W. DeGottardi, E. Waks, and M. Hafezi, New J. Phys. **18**, 113013 (2016).
[22] S. Barik, A. Karasahin, C. Flower, T. Cai, H. Miyake, W. DeGottardi, M. Hafezi, and E. Waks, Science **359**, 666 (2018).
[23] T. Pregnolato, X. L. Chu, T. Schröder, R. Schott, A. D. Wieck, A. Ludwig, P. Lodahl, and N. Rotenberg, APL Photonics **5**, 086101 (2020).
[24] R. E. Christiansen, F. Wang, O. Sigmund, and S. Stobbe, Nanophotonics **8**, 1363 (2019).
[25] H. Pichler, T. Ramos, A. J. Daley, and P. Zoller, Phys. Rev. A **91**, 042116 (2015).
[26] S. Mahmoodian, P. Lodahl, and A. S. Sørensen, Phys. Rev. Lett. **117**, 240501 (2016).

[27] P. St-Jean, V. Goblot, E. Galopin, A. Lemaître, T. Ozawa, L. Le Gratiet, I. Sagnes, J. Bloch, and A. Amo, Nat. Photonics **11**, 651 (2017).

[28] M. Hafezi, E. A. Demler, M. D. Lukin, and J. M. Taylor, Nat. Phys. **7**, 907 (2011).

[29] M. S. Rider, S. J. Palmer, S. R. Pocock, X. Xiao, P. Arroyo Huidobro, and V. Giannini, J. Appl. Phys. **125**, 120901 (2019).

[30] N. Rotenberg and L. Kuipers, Nat. Photonics **8**, 919 (2014).

[31] N. Parappurath, F. Alpeggiani, L. Kuipers, and E. Verhagen, Sci. Adv. **6**, 1 (2020).

[32] J. K. Asbóth, L. Oroszlány, and A. Pályi, *A Short Course on Topological Insulators*, Lecture Notes in Physics Vol. 919 (Springer International Publishing, Cham, 2016), https://link.springer.com/book/10.1007/978-3-319-25607-8.

[33] S. Arora, T. Bauer, R. Barczyk, E. Verhagen, and L. Kuipers, Light Sci. Appl. **10**, 9 (2021).

[34] M. I. Shalaev, W. Walasik, A. Tsukernik, Y. Xu, and N. M. Litchinitser, Nat. Nanotech. **14**, 31 (2018).

[35] X.-T. He, E.-T. Liang, J.-J. Yuan, H.-Y. Qiu, X.-D. Chen, F.-L. Zhao, and J.-W. Dong, Nat. Commun. **10**, 872 (2019).

[36] T. Ma and G. Shvets, New J. Phys. **18**, 025012 (2016).

[37] J. W. Dong, X. D. Chen, H. Zhu, Y. Wang, and X. Zhang, Nat. Mater. **16**, 298 (2017).

[38] M. A. Gorlach, X. Ni, D. A. Smirnova, D. Korobkin, D. Zhirihin, A. P. Slobozhanyuk, P. A. Belov, A. Alù, and A. B. Khanikaev, Nat. Commun. **9**, 909 (2018).

[39] Y. Yang, Y. F. Xu, T. Xu, H. X. Wang, J. H. Jiang, X. Hu, and Z. H. Hang, Phys. Rev. Lett. **120**, 217401 (2018).

[40] Z. Wang, Y. D. Chong, J. D. Joannopoulos, and M. Soljačić, Phys. Rev. Lett. **100**, 013905 (2008).

[41] P. Kaspar, R. Kappeler, D. Erni, and H. Jäckel, Opt. Express **19**, 24344 (2011).

[42] K. Busch, S. Lölkes, R. B. Wehrspohn, and H. Föll, *Photonic Crystals: Advances in Design, Fabrication and Characterization* (John Wiley & Sons, New York, 2006), https://www.wiley.com/en-us/Photonic+Crystals:+Advances+in+Design,+Fabrication,+and+Characterization-p-9783527607174.

[43] See Supplemental Material at http://link.aps.org/supplemental/10.1103/PhysRevLett.128.203903 for more details on the near-field of the topological edge state and the longitudinal and transverse extent of the electric field amplitude along the interface.

[44] P. S. J. Russell, Appl. Phys. B **39**, 231 (1986).

[45] H. Gersen, T. J. Karle, R. J. P. Engelen, W. Bogaerts, J. P. Korterik, N. F. van Hulst, T. F. Krauss, and L. Kuipers, Phys. Rev. Lett. **94**, 123901 (2005).

[46] K. Y. Bliokh and F. Nori, Phys. Rep. **592**, 1 (2015).

[47] A. Aiello, P. Banzer, M. Neugebauer, and G. Leuchs, Nat. Photonics **9**, 789 (2015).

[48] K. Y. Bliokh, D. Smirnova, and F. Nori, Science **348**, 1448 (2015).

[49] A. Y. Bekshaev, K. Y. Bliokh, and F. Nori, Phys. Rev. X **5**, 011039 (2015).

[50] L. Xu, H.-X. Wang, Y.-D. Xu, H.-Y. Chen, and J.-H. Jiang, Opt. Express **24**, 18059 (2016).

[51] H. Gersen, L. Novotny, L. Kuipers, and N. F. Van Hulst, Nat. Photonics **1**, 242 (2007).